

Improved bounds on Lorentz violation from composite pulse Ramsey spectroscopy in a trapped ion

Received: 12 October 2022

Accepted: 8 November 2022

Published online: 27 November 2022

 Check for updatesLaura S. Dreissen¹✉, Chih-Han Yeh¹, Henning A. Fürst^{1,2}, Kai C. Gremse¹ & Tanja E. Mehlstäubler^{1,2}

In attempts to unify the four known fundamental forces in a single quantum-consistent theory, it is suggested that Lorentz symmetry may be broken at the Planck scale. Here we search for Lorentz violation at the low-energy limit by comparing orthogonally oriented atomic orbitals in a Michelson-Morley-type experiment. We apply a robust radiofrequency composite pulse sequence in the $^2F_{7/2}$ manifold of an Yb^+ ion, extending the coherence time from 200 μs to more than 1 s. In this manner, we fully exploit the high intrinsic susceptibility of the $^2F_{7/2}$ state and take advantage of its exceptionally long lifetime. We match the stability of the previous best Lorentz symmetry test nearly an order of magnitude faster and improve the constraints on the symmetry breaking coefficients to the 10^{-21} level. These results represent the most stringent test of this type of Lorentz violation. The demonstrated method can be further extended to ion Coulomb crystals.

The standard model (SM) of particle physics describes non-gravitational interactions between all particles and fields, while gravitation is described by general relativity in a classical manner. Together, they have explained many physical phenomena observed in the universe remarkably well, but an accurate description of gravity at the quantum level is lacking. A number of theories that attempt to unify the SM and gravitation at the Planck scale suggest that breaking of Lorentz symmetry might occur either spontaneously¹ or explicitly^{2–4}. Lorentz symmetry states that the outcome of a local experiment does not depend on the orientation or the velocity of the apparatus⁵. A suppressed effect emerging from Lorentz violation (LV) at the Planck scale could be observed at experimentally accessible energies in the laboratory⁶. Accurate spectroscopic measurements in trapped particles have reached fractional uncertainties beyond the natural suppression factor⁷, which makes a hypothetical LV measurable in such systems. Furthermore, at high energies, LV could be suppressed by super-symmetry⁸. Therefore, accurate low-energy measurements in atoms are suitable to search for LV and complement existing bounds set at high energies with, e.g., particle colliders and astrophysical observations^{9–12}.

Laboratory tests of Lorentz symmetry are based on a similar principle as introduced by Michelson and Morley, who used a rotating interferometer to measure the isotropy of the speed of light¹³. Improved bounds on LV for photons have been realized by a variety of experiments involving high-finesse optical and microwave cavities, see e.g. refs. 5, 14–17. Spectroscopic bounds for protons and neutrons are set using atomic fountain clocks^{18,19} and co-magnetometers^{20,21}. More recently, the bounds on LV in the combined electron-photon sector have been explored using precision spectroscopy in trapped ions^{22–24}. These experiments compare energy levels with differently oriented, relativistic, non-spherical electron orbitals as the Earth rotates. Strong bounds on LV were set with trapped $^{40}\text{Ca}^+$ ions, where a decoherence-free entangled state of two ions in the electronic $^2D_{5/2}$ manifold was created to suppress ambient noise^{22,23}. The relatively short 1.2 s radiative lifetime of the $^2D_{5/2}$ state in Ca^+ and the requirement for high-fidelity quantum gates limit the scalability and, ultimately, the sensitivity of LV tests with this scheme²³. The highly relativistic $^2F_{7/2}$ state in the Yb^+ ion is an order of magnitude more sensitive to LV than the $^2D_{5/2}$ state in Ca^+ ^{25,26} and its radiative lifetime was measured to be about 1.6 years²⁷. However, gate operation on the electronic octupole (E3)

¹Physikalisch-Technische Bundesanstalt, Bundesallee 100, 38116 Braunschweig, Germany. ²Institut für Quantenoptik, Leibniz Universität Hannover, Welfengarten 1, 30167 Hanover, Germany. ✉e-mail: laura.dreissen@ptb.de

transition, required to efficiently populate the $^2F_{7/2}$ manifold, suffers from a low fidelity, making entanglement-based techniques unfeasible. The beneficial properties of Yb^+ were recently partly exploited in a 45-day comparison of two separate state-of-the-art single-ion optical $^{171}\text{Yb}^+$ clocks, both with a fractional uncertainty at the 10^{-18} level, reaching a more than ten-fold improvement²⁴. However, operating the Yb^+ ion as an optical clock limits the experiment to only probe the Zeeman levels that are least sensitive to LV ($m_j = \pm 1/2$).

In this work we present improved bounds on LV in the electron-photon sector using a method that fully exploits the high susceptibility of the stretched $m_j = \pm 7/2$ states in the $^2F_{7/2}$ manifold of Yb^+ and takes advantage of its long radiative lifetime. With a robust radio frequency (rf) spin-echoed Ramsey sequence^{26,28} we populate all Zeeman sublevels in the $^2F_{7/2}$ manifold and make a direct energy comparison between the orthogonally oriented atomic orbitals within a single trapped ion. We decouple the energy levels from noise in the ambient magnetic field to reach a 5000-fold longer coherence time during the Ramsey measurement and extend the dark time to $T_D > 1$ s. With an unprecedented sensitivity to LV, scaling as $\sigma_{\text{LV}} \propto \sqrt{1/T_D N_{\text{ion}}}$, we reduce the required total averaging time by nearly an order of magnitude already with a single ion ($N_{\text{ion}} = 1$). The measurement scheme is simple, robust, scalable and eliminates the requirement of optical clock operation or high-fidelity quantum gates. The rf sequence is insensitive to both temporal and spatial field inhomogeneities and can be applied to a string of N_{ion} trapped ions for an increased sensitivity to LV in the future.

Results

Theoretical framework

The constraints on LV extracted in this work are quantified in the theoretical framework of the standard model extension (SME)²⁹. The SME is an effective field theory in which the SM Lagrangian is extended with all possible terms that are not Lorentz invariant. It is a platform in which LV of all SM particles are described, enabling comparisons between experimental results from many different fields³⁰. In spectroscopic experiments, a violation of Lorentz symmetry can be interpreted as LV of electrons or photons, because there is no preferred reference system. In this work, we interpret the results as a difference in isotropy between photons and electrons, similar as in refs. 22, 24.

LV in the combined electron-photon sector is quantified by adding a symmetry-breaking tensor $c'_{\mu\nu} = c_{\mu\nu} + k_{\mu\nu}/2$ to the SM Lagrangian^{25,29}, where $c_{\mu\nu}$ and $k_{\mu\nu}$ describe LV for electrons and photons, respectively. For simplicity, the prime is omitted throughout the rest of this work and the extracted coefficients are those of the combined $c'_{\mu\nu}$ tensor, which is taken as traceless and symmetric. The components of the $c_{\mu\nu}$ tensor are frame dependent. A unique definition of the symmetry breaking tensor c_{MN} exists in the Sun-centered, celestial, equatorial frame (SCCEF), illustrated in Fig. 1a. In order to make comparisons with other experiments, the $c_{\mu\nu}$ tensor defined in our local laboratory frame is transformed to the SCCEF to constrain the components of the c_{MN} tensor. The full derivation of the transformation can be found in the Supplementary Information.

In a bound electronic systems, LV leads to a small energy shift^{25,26}

$$\delta\mathcal{H} = -\frac{1}{6m_e} C_0^{(2)} T_0^{(2)}, \quad (1)$$

where m_e is the electron mass, the $T_0^{(2)} = \mathbf{p}^2 - 3p_z^2$ operator depends on the direction of the electron's momentum and $C_0^{(2)}$ contains elements of the c_{MN} tensor. For a state with total angular momentum J and projection m_j onto the quantization axis \hat{z} , the matrix element of the $T_0^{(2)}$ operator is given by²⁶

$$\langle J, m_j | T_0^{(2)} | J, m_j \rangle = \frac{-J(J+1) + 3m_j^2}{\sqrt{(2J+3)(J+1)(2J+1)J(2J-1)}} \times (J \parallel T^{(2)} \parallel J). \quad (2)$$

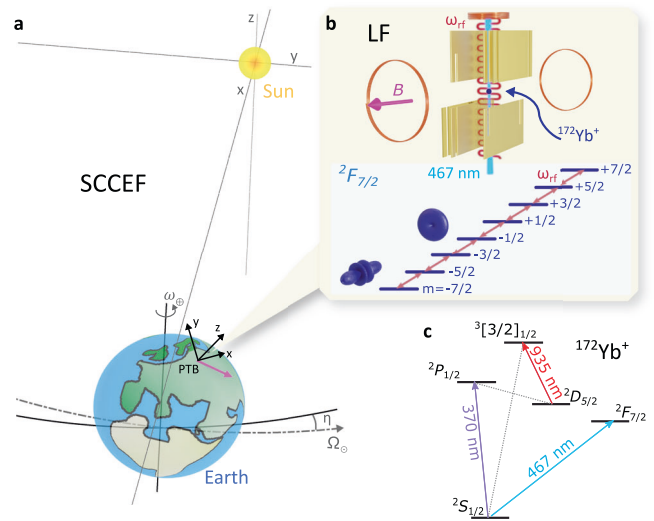


Fig. 1 | A schematic overview of the experimental principle. a In the laboratory frame (LF) coordinate system z points vertically upwards, y points North and x points east. The fixed quantization axis B (pink arrow) in the LF coordinate system lies in the horizontal plane and points 20° south of x and probes different directions in the SCCEF as the Earth rotates around its axis (ω_\oplus) and orbits the Sun (Ω_\odot). **b** In the LF a single $^{172}\text{Yb}^+$ ion is trapped in a segmented rf trap. Two coils generate a quantization field of $221 \mu\text{T}$. The electron orbitals of the $m_j = \pm 1/2$ and $m_j = \pm 7/2$ Zeeman sublevels in the $^2F_{7/2}$ state orient themselves orthogonally to each other. The $^2F_{7/2}$ state is populated via the E3 transition near 467 nm . The m_j substates are coupled via the rf magnetic field at ω_{rf} created with a coil that is placed 5.5 cm above the ion. **c** A simplified energy level diagram of $^{172}\text{Yb}^+$, showing the optical E3 transition and the transitions near 370 nm and 935 nm used for Doppler cooling and state detection.

Equations (1) and (2) show that in the SCCEF, LV manifests itself as an energy shift that modulates with Earth's rotation frequency. The magnitude of this shift is dependent on both m_j^2 and the reduced matrix element $\langle J \parallel T^{(2)} \parallel J \rangle$. The value of the latter is particularly high for the $^2F_{7/2}$ manifold in the Yb^+ ion^{25,26}. The goal of this experiment is to test LV in a single trapped $^{172}\text{Yb}^+$ ion by measuring the energy difference between m_j substates in the $^2F_{7/2}$ manifold as the Earth rotates.

Measurement principle

The experiment is performed with a single ion, stored in a linear rf Paul-trap, see Fig. 1b. It is cooled to the Doppler limit of about 0.5 mK on the dipole allowed transition near a wavelength of 370 nm , assisted by a repumper near 935 nm . A set of coils is used to define the quantization axis of $B = 221 \mu\text{T}$, which lies in the horizontal plane with respect to Earth's surface and points 20° south of east, see Fig. 1a. Active feedback is applied on auxiliary coils in three directions to stabilize the magnetic field. The $^2F_{7/2}$ state can be efficiently populated via coherent excitation of the highly-forbidden electric octupole (E3) transition (Fig. 1c) using an ultra-stable frequency-doubled laser at 934 nm ³¹, which is either stabilized only to a cryogenic silicon cavity via a frequency comb³² or, optionally, to the single-ion optical $^{171}\text{Yb}^+$ clock³³. A Rabi frequency of $\Omega_{\text{E3}}/2\pi = 10 \text{ Hz}$ is achieved on the E3 transition. More details on the experimental apparatus can be found in the Methods section.

The free evolution of a substate $|^2F_{7/2}, m_j\rangle$ interacting with a magnetic field $\mathbf{B} \equiv B_z \hat{z}$, is given by the Hamiltonian $\mathcal{H}_{\text{free}} = \mathcal{H}_{\text{lin}} + \mathcal{H}_{\text{quad}} = \mu B_z J_z + \kappa J_z^2$, where μ is the magnetic moment. The quadratic term in the Hamiltonian gives rise to an energy shift according to $E_{m_j}/h \equiv \kappa/2\pi \times m_j^2$. The value of $\kappa = \kappa_q + \kappa_{\text{LV}}$ is dependent on the quadrupole shift for the trapped ion in the $^2F_{7/2}$ state and a possible shift due to LV, respectively. The contribution from LV to κ is

given by²⁶

$$\frac{\kappa_{LV}}{2\pi} = 5.1 \times 10^{15} \text{ Hz} \times C_0^{(2)}, \quad (3)$$

where $C_0^{(2)}$ contains components of the c_{MN} tensor in the SCCEF, see the Supplementary Information.

A modulation of the quadratic contribution to the Zeeman splitting in the $^2F_{7/2}$ manifold is measured with rf spectroscopy. The m_j levels are coupled via a rf magnetic field supplied to the ion by a resonant LC circuit. The coupling term in the Hamiltonian is given by $\mathcal{H}_{\text{coupling}} = \Omega_F \cos(\omega_{\text{rf}}t + \phi) J_x$, where $\Omega_F/2\pi = 33$ kHz is the multilevel Rabi frequency and ω_{rf} and ϕ are the frequency and the phase of the rf field, respectively. The rf frequency is close to resonance with the, to first order, equidistant m_j levels given by $\omega_{\text{rf}}/2\pi = \mu B_j/h + \delta(t)/2\pi \approx 3.5$ MHz, where $\delta(t)$ is a small detuning from temporal drifts in the ambient magnetic field. The full Hamiltonian of the system in the interaction picture after applying the rotating wave approximation is given by

$$\mathcal{H} = \delta(t) J_z + \kappa J_z^2 + \Omega_F [J_x \cos(\phi) - J_y \sin(\phi)], \quad (4)$$

where the changes in $\delta(t)$ and κ should be much slower than the π -pulse time of $t_\pi = \pi/\Omega_F = 15$ μ s.

A composite rf pulse sequence, based on a spin-echoed Ramsey scheme, is implemented to mitigate the influence of $\delta(t)$, while retaining a high sensitivity to variations of κ . A schematic overview of the rf sequence is shown in Fig. 2 a. Starting from either one of the $m_j = \pm 1/2$ states, a $\pi/2$ -pulse, i.e. $t_{\pi/2} = t_\pi/2$, with phase $\phi = 0$ spreads the population over all the Zeeman sublevels. A modulation sequence, consisting of ten repetitions of the form $[t_w] - [t_\pi(\phi_i)] - [t_w]$, is applied to cancel dephasing from $\delta(t)$. Here t_w is the time in which the state freely evolves and $t_\pi(\phi_i)$ indicates a π -pulse with phase ϕ_i . In our experimental environment, dephasing is successfully canceled for $t_w = 100$ μ s. The phases ϕ_i of the consecutive π -pulses are set to (0,4,2,4,0,0,4,2,4,0) $\pi/5$, for which the modulation sequence is shown to be highly robust against pulse errors from, e.g., detuning and intensity variations²⁸. At the end of the sequence, a $\pi/2$ -pulse with phase $\phi = \pi$ retrieves a fraction P_f of the population back into the initial $m_j = \pm 1/2$ state. The Ramsey dark-time, i.e. the time in which the state freely evolves, can be extended to $T_D = N \times 20 t_w$ by repeating the modulation sequence N times.

The retrieved fraction P_f is dependent on the phase κT_D acquired during the free-evolution time, which stems from the quadratic term in the Hamiltonian of Eq. (4). Therefore, κ_{LV} can be extracted from a measurement of P_f at a fixed T_D . Since a hypothetical LV would manifest itself as a modulation of κ at frequencies related to a sidereal day ($\omega_\oplus/2\pi = 1/23.934$ h), a signal of LV is characterized by oscillations of P_f at the same modulation frequencies. A measurement of P_f is realized by de-exciting the ion via the E3 transition to the $^2S_{1/2}$ state, where it can be detected by collecting fluorescence on the dipole allowed $^2S_{1/2} \rightarrow ^2P_{1/2}$ transition.

The highest measurement accuracy is achieved when the measured quantity P_f is most sensitive to variations of κ , i.e. $|dP_f/d\kappa|$, is maximized, which is the case at $\kappa T_D = 0.15$ rad²⁶. Using the axial secular frequency of 266(5) kHz set during the measurement campaign and the quadrupole moment of the $^2F_{7/2}$ state³⁴, κ_q was calculated to be 0.13(3) rad s⁻¹, see the Supplementary Information. The corresponding optimal Ramsey dark time is $T_D = 1.15$ s.

Experimental sequence

A schematic overview of the full experimental sequence is shown in Fig. 2b. Stable long-term operation of the experiment is required to resolve oscillation periods related to a potential LV, i.e. at 11.967 and 23.934 hours. Especially the center frequency of the E3 transition is

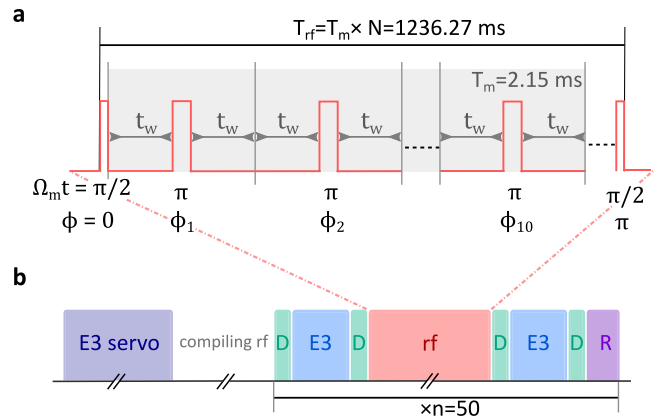


Fig. 2 | Pulse sequences. **a** The applied composite rf pulse sequence is a more robust version of a spin-echoed Ramsey scheme. A Ramsey sequence of $T_{\text{rf}} = 1236.27$ ms starts and ends with a $\pi/2$ -pulse. A 2.15 ms-long modulation sequence of 10 π -pulses with phases ϕ_i ($i = 1 \dots 10$), each spaced by $2t_w = 200$ μ s, is repeated $N = 575$ times to cancel dephasing due to ambient magnetic field noise. The phases ϕ_i are chosen such (see text) that the sequence is robust against pulse errors. **b** Every $n = 50$ measurements, a 4-point servo sequence (E3 servo) of 40 s is applied to follow the E3 center frequency, after which the rf sequence is compiled for 2.5 s. The measurement sequence consists of two 50 ms-long E3 pulses (E3), the rf pulse sequence (rf) of 1236.27 ms, four detection pulses (D) of 2.5 ms and a sequence at the end of 20 ms for state preparation (R) for the next measurement run. During post-selection, the data points are considered valid if the ion was in the desired state during the first three detection pulses.

sensitive to external perturbations from, e.g., magnetic field drifts and intensity fluctuations. Therefore, a 4-point servo-sequence of two opposite Zeeman transitions $|^2S_{1/2}, m_j = \pm 1/2\rangle \rightarrow |^2F_{7/2}, m_j = \pm 1/2\rangle$ at half the linewidth is applied every $n = 50$ measurement runs to follow the E3 center frequency. For details on this technique, see e.g. ref. 35. On average a population transfer of 80% is realized to the $^2F_{7/2}$ state via the E3 transition using the servo-sequence.

After the E3 servo and 2.5 s of compilation time for the rf pulse sequence, a measurement starts with a detection pulse to determine if the ion is cooled and prepared in the correct initial $|^2S_{1/2}, m_j = \pm 1/2\rangle$ state. If this is not the case, consecutive repumping and recooling sequences are applied. To save overhead time, either the $|^2F_{7/2}, m_j = +1/2\rangle$ or the $|^2F_{7/2}, m_j = -1/2\rangle$ state is populated via E3 excitation of the same Zeeman transition as was addressed last by the servo sequence. Another detection pulse is applied to determine if the E3 excitation was successful. A single rf modulation sequence of $T_m = 10 \times t_\pi + 20 \times t_w = 2.15$ ms is repeated $N = 575$ times to reach $T_D = 1.15$ s. The full rf sequence runs for $T_{\text{rf}} = N \times T_m + 2 \times t_{\pi/2} = 1236.27$ ms. A third detection pulse is applied to determine if the ion was quenched to the ground state during the rf sequence due to, e.g., a collision with background gas. The ion is de-excited on the E3 transition and, with a final detection pulse, P_f is measured. At the end of the measurement sequence, the ion is re-cooled and prepared in the required $|^2S_{1/2}, m_j = \pm 1/2\rangle$ electronic ground state for the next measurement run. Data points are only considered valid when the ion was in the correct state at both the second and the third detection stage. After post-selection of valid data points an average contrast of 0.77(6) is reached. Including additional overhead from compilation time, data points are obtained at a rate of 1/191 s⁻¹.

Bounds on Lorentz violation

The data acquired over a period of 912 h, with an up-time of 591 h, is shown in Fig. 3a. Data points are averaged in equidistant bins of 15 min. The measured population is decomposed in two parts $P_f = P(\kappa_q) + P(\kappa_{LV})$, where $P(\kappa_q)$ gives rise to a constant offset of $P_0 = 0.39$ and $P(\kappa_{LV}) = dP_f/d\kappa \times \kappa_{LV}$ contains a potential LV signal. To extract κ_{LV} from

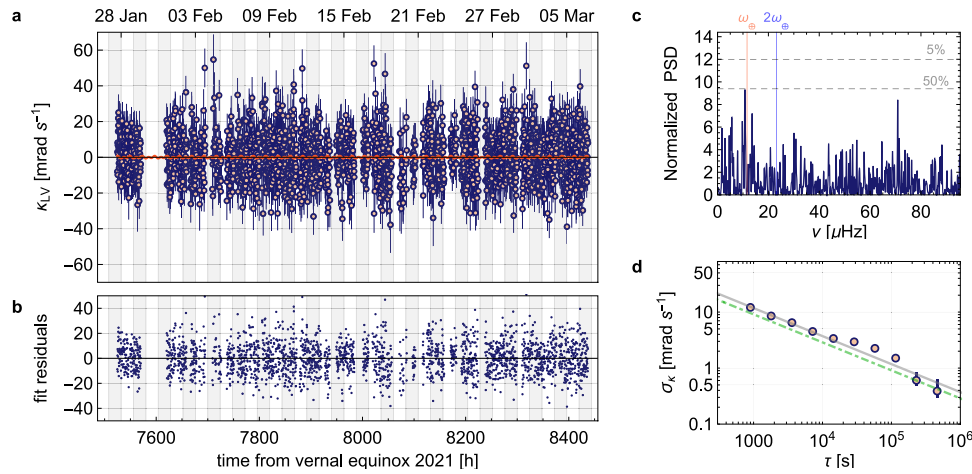


Fig. 3 | Data acquired over a period of 912 h with an up-time of 591 h. **a** The measured value of κ_{LV} (blue data points) extracted from the retrieved population P_f . Data points are binned at 15 min intervals. The error bars reflect the standard error (1σ) from quantum projection noise. The data is fitted to Eq. (5) (red line) from which bounds are set on components of the c_{MN} tensor. **b** The residuals of the fit with a reduced $\chi^2 = 0.92$. **c** A Lomb–Scargle periodogram for spectral analysis of irregularly spaced data. The normalized power spectral density is plotted for frequencies between 0 and 100 μHz . The vertical lines indicate the sidereal day

frequency, ω_\oplus , (red) and its second harmonic, $2\omega_\oplus$, (blue). The dashed lines indicate the statistical significance level, i.e. p -value, of the peaks³⁶. **d** The Allan deviation, σ_κ , of the data points shown in **a** as a function of averaging time, τ . The error bars correspond to the standard error to the data, the stability is extracted to be $\sigma_\kappa = 372(9)$ $\text{mrad s}^{-1} \tau^{-1/2}$. The expected stability from quantum projection noise (dashed-dotted green line) is 29(3)% lower.

P_f , a high-pass filter is applied with a cutoff frequency of $\nu_c = 5 \mu\text{Hz}$, removing P_0 and slow variations ($\tau_{\text{drift}} < 2.5$ days) caused by drifts in the E3 excitation probability, and the slope $dP_f/dk|_{k=0.13(3)} = -4.4(4)$ is calculated. More details on the data handling and the measurement sensitivity can be found in the Supplementary Information.

In search of LV at Fourier frequencies of ω_\oplus and $2\omega_\oplus$, the data is fitted globally to the fit function

$$\kappa_{LV} = 2\pi \times 5.1 \times 10^{15} \times \left[-3 \sin(2\chi) c_{XZ} \cos(\omega_\oplus T) - 3 \sin(2\chi) c_{YZ} \sin(\omega_\oplus T) - \frac{3}{2} c_{X-Y} \sin^2(\chi) \cos(2\omega_\oplus T) - 3 c_{XY} \sin^2(\chi) \sin(2\omega_\oplus T) \right], \quad (5)$$

from which the individual components of the c_{MN} tensor in the SCCEF are extracted, where $c_{X-Y} = c_{XX} - c_{YY}$. The fit overlays the data in Fig. 3a and the residuals from the fit are shown in Fig. 3b, from which the reduced chi-square of $\chi^2 = 0.92$ is extracted. The fitted values of the components of the c_{MN} tensor are given in Table 1. For comparison, the values obtained in refs. 23, 24 are also presented. The uncorrelated linear combination of the fit parameters, calculated by diagonalizing the covariance matrix, are given in Table 2. The spectral content of the data, shown in Fig. 3c, is analyzed using a Lomb–Scargle periodogram³⁶, which is specifically suited for spectral analysis of irregularly spaced data. The statistical significance level, i.e. p -values³⁶, of 50% and 95% are indicated by horizontal lines.

The fit results show that the extracted values for c_{X-Y} , c_{XZ} and c_{YZ} are consistent with zero within a 1σ uncertainty. Only c_{XY} shows a 1.1σ deviation from zero, but spectral analysis does not show a significant Fourier component at $2\omega_\oplus$. Therefore, we conclude that we do not find evidence of LV, in agreement with previous work^{23,24}. The stability of the data points is analyzed by calculating the Allan deviation, as shown in Fig. 3d. The data averages down as $\sigma_\kappa = 372(9)$ $\text{mrad s}^{-1} \tau^{-1/2}$, which is 29(3)% higher than what is expected from quantum projection noise.

Discussion

The presented results set the most stringent bounds on this type of LV in the combined electron-photon sector. With the presented method, the resolution of the previous most sensitive measurement²⁴ is reached 9 times faster. We improve on the state-of-the-art by a factor of 2.2 and constrain all the coefficients of the c_{MN} tensor now at the 10^{-21} level. Due to the experimental geometry, a higher sensitivity is reached for signals that oscillate at $2\omega_\oplus$ than those that oscillate at ω_\oplus , see the Supplementary Information. Therefore, the tightest constraint of 3.9×10^{-21} is achieved on c_{XY} .

In this work, coefficients of the first and second harmonic order of the sidereal day modulation frequency were considered. However, due to the high total angular momentum of the $^2F_{7/2}$ state, the applied method is sensitive to LV at harmonics of up to sixth order^{37,38}. Therefore, in combination with improved many-body calculations, experimental constraints can be translated into bounds on a larger number of coefficients in the future³⁸.

Table 1 | The symmetry breaking tensor components

Correlated LV parameters	This work	¹⁷¹ Yb ⁺ limits ²⁴	⁴⁰ Ca ⁺ limits ²³
c_{X-Y}	$(-5.2 \pm 7.8) \times 10^{-21}$	$(-0.5 \pm 1.7) \times 10^{-20}$	$(6.2 \pm 9.2) \times 10^{-19}$
c_{XY}	$(4.4 \pm 3.9) \times 10^{-21}$	$(-7.0 \pm 8.1) \times 10^{-21}$	$(2.4 \pm 4.8) \times 10^{-19}$
c_{XZ}	$(-5.0 \pm 9.3) \times 10^{-21}$	$(0.8 \pm 1.3) \times 10^{-20}$	$(0.8 \pm 2.1) \times 10^{-19}$
c_{YZ}	$(6.3 \pm 8.9) \times 10^{-21}$	$(1.0 \pm 1.3) \times 10^{-20}$	$(-3.1 \pm 2.2) \times 10^{-19}$

The correlated components of the c_{MN} tensor extracted from the fit shown in Fig. 3a, compared to existing limits from refs. 23, 24. All uncertainties represent a 1σ interval.

Table 2 | The uncorrelated combination of symmetry breaking tensor components

Uncorrelated linear combinations of parameters	This work
$0.70c_{XZ} + 0.26c_{YZ} + 0.51c_{X-Y} + 0.42c_{XY}$	$(0.0 \pm 1.0) \times 10^{-20}$
$0.24c_{XZ} - 0.61c_{YZ} + 0.46c_{X-Y} - 0.59c_{XY}$	$(-13.8 \pm 9.6) \times 10^{-21}$
$-0.47c_{XZ} - 0.50c_{YZ} + 0.38c_{X-Y} + 0.62c_{XY}$	$(3.0 \pm 7.2) \times 10^{-21}$
$-0.48c_{XZ} + 0.56c_{YZ} + 0.61c_{X-Y} - 0.29c_{XY}$	$(-0.4 \pm 3.5) \times 10^{-21}$

The covariance matrix from the fit shown in Fig. 3a is diagonalized to obtain the linear combination of parameters of the c_{MN} tensor. All uncertainties represent a 1σ interval.

The method demonstrated in this work is technically less demanding and more robust than alternative methods requiring simultaneous operation of independent optical clocks or high-fidelity entanglement gates^{23,24}. It is applicable in a wide variety of systems, e.g., highly-charged ions or ultra-cold atoms²⁶ and it is capable of scaling to multiple N_{ion} ions in linear ion Coulomb crystals for a further enhancement of the sensitivity. Up-scaling with an entanglement-based techniques²³ is technically demanding when considering the ${}^2F_{7/2}$ state in Yb^+ due to the low-fidelity (p) single ion gate on the E3 transition, which further deteriorates, according to $p^{N_{\text{ion}}}$, for larger ion numbers. In contrast, the implemented composite rf pulse sequence is highly robust against errors originating from spatial and temporal fluctuations of both the ambient field and the rf field. Therefore, the coherence time is not expected to significantly decrease for larger ion numbers and a $\sqrt{N_{\text{ion}}}$ higher sensitivity is expected in such a system. Moreover, the long radiative lifetime of the ${}^2F_{7/2}$ state²⁷ does not significantly limit the coherence time and, with several technical improvements, longer interrogation times could be reached. Note that for efficient population transfer via the E3 transition, advanced cooling techniques, such as EIT³⁹ or Sisyphus cooling^{40,41}, might be advantageous in larger ion crystals. With the presented method, the boundaries of Lorentz symmetry tests can be pushed to the 10^{-22} level with a string of 10 Yb^+ ions in the future.

Methods

Experimental details

A single ${}^{172}\text{Yb}^+$ ion is trapped in a segmented rf Paul-trap^{42,43}. The radial confinement is set with an rf electric field supplied by a resonant circuit at a frequency of $\Omega_{\text{rf}}/2\pi = 24.38 \text{ MHz}$, while the axial confinement is set by dc voltages supplied to the trapping segment and the neighboring segments. With the applied confinement, the secular frequencies are $\omega(\text{rad1, rad2, ax})/2\pi = (775, 510, 266) \text{ kHz}$. Micromotion is measured on a daily basis with the photon correlation technique⁴⁴ and compensated in three directions to typically $E_{\text{rf}} < 100 \text{ V/m}$. The quantization field of $\mathbf{B} = 221 \mu\text{T}$ lies in the horizontal plane under an angle of 25° to the trap axis. The \mathbf{B} -field is measured with a sensor near the vacuum chamber and active feedback is applied in three orthogonal directions via current modulation of six auxiliary coils.

The ion is cooled to approximately 0.5 mK , close to the Doppler limit, on the dipole allowed ${}^2S_{1/2} \rightarrow {}^2P_{1/2}$ transition assisted by a repumper laser near 935 nm . Fluorescence from the decay of the ${}^2P_{1/2}$ state is collected by a lens of $N/A = 0.27$ and imaged onto the electron-multiplying charge-coupled device (EMCCD) camera⁴⁵. This enables state detection via the electron shelving technique. The ion can be prepared in either the $|{}^2S_{1/2}, m_j = -1/2\rangle$ or the $|{}^2S_{1/2}, m_j = +1/2\rangle$ state using circular polarized beam near 370 nm pointing along the direction of the quantization axis. The 467 nm laser for excitation on the E3 transition lies in the radial plane and its beam waist is $26(3) \times 38(3) \mu\text{m}$ at the ion. The power is stabilized to $6.0(2) \text{ mW}$, at which a Rabi frequency of $\Omega_{\text{E3}}/2\pi = 10 \text{ Hz}$ is reached. The light is frequency-shifted and pulsed using acousto-optic modulators.

The resonant rf coil, consisting of 27 turns wound at a diameter of 4.5 cm , is placed 5.5 cm above the ion. The resonance frequency of the coil is $\omega_{\text{res}}/2\pi = 3.5147(7) \text{ MHz}$ and it is driven by a signal derived from a direct digital synthesizer (DDS), referenced to a stable 100 MHz signal from a hydrogen maser. At $221 \mu\text{T}$, the resonance frequency between the m_j levels in the ${}^2F_{7/2}$ state is $\omega_{\text{rf}}/2\pi = 3.52 \text{ MHz}$, close to the resonance frequency of the coil. The achieved multi-level Rabi frequency is $\Omega_{\text{rf}}/2\pi = 33 \text{ kHz}$. The ambient magnetic field is monitored throughout the measurement campaign via data acquired in the E3 servo sequence. Drifts are observed at the level of 100 nT , corresponding to a detuning $\Delta\omega_{\text{rf}}/2\pi = 1.6 \text{ kHz}$. The frequency supplied to the coil is actively adjusted to remain in resonance with the frequency given by the linear Zeeman splitting. For this purpose, the resonance frequency as a function of magnetic field was calibrated to be

$\omega_{\text{rf}}(B)/2\pi = [1.581(1.6)B + 0.0162(3)]$ in MHz. For further details on the experimental set-up, see refs. 31, 42, 45, 46.

Data availability

The source data generated in this study are provided in the Source Data file. Source data are provided with this paper.

Code availability

Reasonable requests for computer code should be addressed to the corresponding author.

References

- Kostelecký, V. A. & Samuel, S. Spontaneous breaking of Lorentz symmetry in string theory. *Phys. Rev. D* **39**, 683–685 (1989).
- Horava, P. Quantum gravity at a Lifshitz point. *Phys. Rev. D* **79**, 084008 (2009).
- Pospelov, M. & Shang, Y. Lorentz violation in Horava-Lifshitz-type theories. *Phys. Rev. D* **85**, 105001 (2012).
- Cognola, G., Myrzakulov, R., Sebastiani, L., Vagnozzi, S. & Zerbini, S. Covariant Horava-like and mimetic Horndeski gravity: cosmological solutions and perturbations. *Class. Quantum Gravity* **33**, 225014 (2016).
- Tobar, M. E., Wolf, P., Bize, S., Santarelli, G. & Flambaum, V. Testing local Lorentz and position invariance and variation of fundamental constants by searching the derivative of the comparison frequency between a cryogenic sapphire oscillator and hydrogen maser. *Phys. Rev. D* **81**, 022003 (2010).
- Mattingly, D. Modern tests of Lorentz invariance. *Living Rev. Relativ.* **8**, 5 (2005).
- Kostelecký, V. A. & Potting, R. CPT, strings, and meson factories. *Phys. Rev. D* **51**, 3923–3935 (1995).
- Nibbelink, S. G. & Pospelov, M. Lorentz violation in supersymmetric field theories. *Phys. Rev. Lett.* **94**, 081601 (2005).
- Abazov, V. M. et al. Search for violation of Lorentz invariance in top quark pair production and decay. *Phys. Rev. Lett.* **108**, 261603 (2012).
- Aaij, R. et al. Search for violations of Lorentz invariance and CPT symmetry in $B_{(s)}^0$ mixing. *Phys. Rev. Lett.* **116**, 241601 (2016).
- Schreck, M. Vacuum Cherenkov radiation for Lorentz-violating fermions. *Phys. Rev. D* **96**, 095026 (2017).
- Albert, A. et al. Constraints on Lorentz invariance violation from HAWC observations of gamma rays above 100 TeV . *Phys. Rev. Lett.* **124**, 131101 (2020).
- Michelson, A. A. & Morley, E. W. Influence of motion of the medium on the velocity of light. *Am. J. Sci.* **s3-31**, 377–385 (1886).
- Herrmann, S. et al. Rotating optical cavity experiment testing Lorentz invariance at the 10^{-17} level. *Phys. Rev. D* **80**, 105011 (2009).
- Müller, H., Herrmann, S., Braxmaier, C., Schiller, S. & Peters, A. Modern Michelson-Morley experiment using cryogenic optical resonators. *Phys. Rev. Lett.* **91**, 020401 (2003).
- Eisele, C., Nevsky, A. Y. & Schiller, S. Laboratory test of the isotropy of light propagation at the 10^{-17} level. *Phys. Rev. Lett.* **103**, 090401 (2009).
- Safronova, M. S. et al. Search for new physics with atoms and molecules. *Rev. Mod. Phys.* **90**, 025008 (2018).
- Wolf, P., Chapelet, F., Bize, S. & Clairon, A. Cold atom clock test of Lorentz invariance in the matter sector. *Phys. Rev. Lett.* **96**, 060801 (2006).
- Pihan-Le Bars, H. et al. Lorentz-symmetry test at Planck-scale suppression with nucleons in a spin-polarized ${}^{133}\text{Cs}$ cold atom clock. *Phys. Rev. D* **95**, 075026 (2017).
- Brown, J. M., Smullin, S. J., Kornack, T. W. & Romalis, M. V. New limit on Lorentz- and CPT-violating neutron spin interactions. *Phys. Rev. Lett.* **105**, 151604 (2010).
- Smiciklas, M., Brown, J. M., Cheuk, L. W., Smullin, S. J. & Romalis, M. V. New test of local Lorentz invariance using a ${}^{21}\text{Ne}$ -Rb-K comagnetometer. *Phys. Rev. Lett.* **107**, 171604 (2011).

22. Pruttivarasin, T. et al. Michelson–Morley analogue for electrons using trapped ions to test Lorentz symmetry. *Nature* **517**, 592–595 (2015).
23. Megidish, E., Broz, J., Greene, N. & Häffner, H. Improved test of local Lorentz invariance from a deterministic preparation of entangled states. *Phys. Rev. Lett.* **122**, 123605 (2019).
24. Sanner, C. et al. Optical clock comparison for Lorentz symmetry testing. *Nature* **567**, 204–208 (2019).
25. Dzuba, V. A. et al. Strongly enhanced effects of Lorentz symmetry violation in entangled Yb^+ ions. *Nature Phys.* **12**, 465–468 (2016).
26. Shaniv, R. et al. New methods for testing Lorentz invariance with atomic systems. *Phys. Rev. Lett.* **120**, 103202 (2018).
27. Lange, R. et al. Lifetime of the $^2F_{7/2}$ level in Yb^+ for spontaneous emission of electric octupole radiation. *Phys. Rev. Lett.* **127**, 213001 (2021).
28. Genov, G. T., Schraft, D., Vitanov, N. V. & Halfmann, T. Arbitrarily accurate pulse sequences for robust dynamical decoupling. *Phys. Rev. Lett.* **118**, 133202 (2017).
29. Colladay, D. & Kostelecký, V. A. Lorentz-violating extension of the Standard Model. *Phys. Rev. D* **58**, 116002 (1998).
30. Kostelecký, V. A. & Russell, N. Data tables for Lorentz and CPT violation. *Rev. Mod. Phys.* **83**, 11–31 (2011).
31. Fürst, H. A. et al. Coherent excitation of the highly forbidden electric octupole transition in $^{172}\text{Yb}^+$. *Phys. Rev. Lett.* **125**, 163001 (2020).
32. Matei, D. G. et al. 1.5 μm lasers with sub-10 mHz linewidth. *Phys. Rev. Lett.* **118**, 263202 (2017).
33. Huntemann, N., Sanner, C., Lipphardt, B., Tamm, C. & Peik, E. Single-ion atomic clock with 3×10^{-18} systematic uncertainty. *Phys. Rev. Lett.* **116**, 063001 (2016).
34. Lange, R. et al. Coherent suppression of tensor frequency shifts through magnetic field rotation. *Phys. Rev. Lett.* **125**, 143201 (2020).
35. Ludlow, A. D., Boyd, M. M., Ye, J., Peik, E. & Schmidt, P. O. Optical atomic clocks. *Rev. Mod. Phys.* **87**, 637–701 (2015).
36. Glynn, E. F., Chen, J. & Mushegian, A. R. Detecting periodic patterns in unevenly spaced gene expression time series using Lomb-Scargle periodograms. *Bioinformatics* **22**, 310–316 (2005).
37. Kostelecký, V. A. & Vargas, A. J. Lorentz and CPT tests with clock-comparison experiments. *Phys. Rev. D* **98**, 036003 (2018).
38. Vargas, A. J. Overview of the phenomenology of Lorentz and CPT violation in atomic systems. *Symmetry* **11**, 1433 (2019).
39. Morigi, G., Eschner, J. & Keitel, C. H. Ground state laser cooling using electromagnetically induced transparency. *Phys. Rev. Lett.* **85**, 4458–4461 (2000).
40. Ejtemaee, S. & Haljan, P. C. 3D Sisyphus cooling of trapped ions. *Phys. Rev. Lett.* **119**, 043001 (2017).
41. Joshi, M. K. et al. Polarization-gradient cooling of 1D and 2D ion Coulomb crystals. *N. J. Phys.* **22**, 103013 (2020).
42. Pyka, K., Herschbach, N., Keller, J. & Mehlstäubler, T. E. A high-precision segmented Paul trap with minimized micromotion for an optical multiple-ion clock. *Appl. Phys. B* **114**, 231–241 (2014).
43. Keller, J. et al. Probing time dilation in Coulomb crystals in a high-precision ion trap. *Phys. Rev. Appl.* **11**, 011002 (2019).
44. Keller, J., Partner, H. L., Burgermeister, T. & Mehlstäubler, T. E. Precise determination of micromotion for trapped-ion optical clocks. *J. Appl. Phys.* **118**, 104501 (2015).
45. Pyka, K. *High-precision ion trap for spectroscopy of Coulomb crystals*. Ph.D. thesis (Leibniz Universität Hannover, Hanover, Germany, 2013).
46. Kalincev, D. et al. Motional heating of spatially extended ion crystals. *Quantum Sci. Technol.* **6**, 034003 (2021).

Acknowledgements

We thank Melina Filzinger, Richard Lange, Burkhard Lipphardt, Nils Huntemann and André Kulosa for experimental support. We thank Ralf Lehnert, Arnaldo Vargas, Nils Huntemann and Ekkehard Peik for helpful discussions and Ravid Shaniv for motivating this work. We thank Ralf Lehnert for carefully reading the manuscript. L.S.D. acknowledges support from the Alexander von Humboldt foundation. This project has been funded by the Deutsche Forschungsgemeinschaft (DFG, German Research Foundation) under Germany's Excellence Strategy - EXC-2123 QuantumFrontiers -390837967 (RU B06) and through Grant No. CRC 1227 (DQ-mat, project B03). This work has been supported by the Max-Planck-RIKEN-PTB-Center for Time, Constants and Fundamental Symmetries.

Author contributions

Conception of the experiment and development of methods: L.S.D., C-H.Y., H.A.F., K.C.G., T.E.M. Design and construction of experimental apparatus: L.S.D., C-H.Y., H.A.F., T.E.M. Data acquisition and analysis: L.S.D., C-H.Y. Preparation and discussion of the manuscript: L.S.D., C-H.Y., H.A.F., K.C.G., T.E.M.

Funding

Open Access funding enabled and organized by Projekt DEAL.

Competing interests

The authors declare no competing interests.

Additional information

Supplementary information The online version contains supplementary material available at <https://doi.org/10.1038/s41467-022-34818-0>.

Correspondence and requests for materials should be addressed to Laura S. Dreissen.

Peer review information *Nature Communications* thanks the anonymous reviewer(s) for their contribution to the peer review of this work.

Reprints and permissions information is available at <http://www.nature.com/reprints>

Publisher's note Springer Nature remains neutral with regard to jurisdictional claims in published maps and institutional affiliations.

Open Access This article is licensed under a Creative Commons Attribution 4.0 International License, which permits use, sharing, adaptation, distribution and reproduction in any medium or format, as long as you give appropriate credit to the original author(s) and the source, provide a link to the Creative Commons license, and indicate if changes were made. The images or other third party material in this article are included in the article's Creative Commons license, unless indicated otherwise in a credit line to the material. If material is not included in the article's Creative Commons license and your intended use is not permitted by statutory regulation or exceeds the permitted use, you will need to obtain permission directly from the copyright holder. To view a copy of this license, visit <http://creativecommons.org/licenses/by/4.0/>.

© The Author(s) 2022